

A new global nonlinear force-free coronal magnetic-field extrapolation code implemented on a Yin-Yang grid

Argyrios Koumtzis (✉ koumtzis@mps.mpg.de)

Max Planck Institute for Solar System Research

Thomas Wiegelmann

Max Planck Institute for Solar System Research

Research Article

Keywords: Magnetic Fields, Corona, Magnetic fields, Models

Posted Date: June 21st, 2022

DOI: <https://doi.org/10.21203/rs.3.rs-1754346/v1>

License:  This work is licensed under a Creative Commons Attribution 4.0 International License.

[Read Full License](#)

A new global nonlinear force-free coronal magnetic-field extrapolation code implemented on a Yin-Yang grid

Argyrios Koumtzis¹ · Thomas Wiegelmann¹

© Springer ●●●

Abstract The solar magnetic field dominates and structures the solar coronal plasma. Detailed insights into the coronal magnetic field are important to understand most of the physical phenomena there. While direct routine measurements of the coronal magnetic field are not available, field extrapolation of the photospheric vector field measurements into the corona is the only way to study the structure and dynamics of the coronal field. Here we focus on global coronal structures which are traditionally modelled using spherical grids and synoptic vector magnetograms as boundary conditions. We developed a new code that performs nonlinear force-free magnetic field extrapolations in spherical geometry. Our new implementation is based on a well-established optimization principle, which was implemented on a Cartesian grid and a single spherical finite-difference grid. In the present work, for the first time, the algorithm is able to reconstruct the magnetic field in the entire corona, including the polar regions. The finite-difference numerical scheme that was employed in previous spherical code versions suffered from numerical inefficiencies because of the convergence of those grids on the poles. In our new code, we implement the so-called Yin-Yang overhead grid, the structure of which addresses this difficulty. Consequently, both the speed and accuracy of the optimization algorithm are improved compared to the previous implementations. We tested our new code using the well known semi-analytical model (Low and Lou solution), which has frequently been used as a benchmark for nonlinear force-free extrapolation codes.

Keywords: Magnetic fields, Corona; Magnetic fields, Models

1. Introduction

Reconstructing the global coronal magnetic field of the Sun remains an open research problem in solar physics. The magnetic structure and topology in the solar atmosphere is of major importance in modelling and understanding the dynamics of the solar corona as phenomena like solar flares and coronal mass ejections are driven by coronal magnetic activity. Our understanding and our ability to model and predict such phenomena require a highly accurate

✉ Wiegelmann
wiegelmann@mps.mpg.de
Koumtzis
koumtzis@mps.mpg.de

¹ Max-Planck-Institut für Sonnensystemforschung, Justus-von-Liebig-Weg 3, 37077 Göttingen, Germany

coronal magnetic field model. The progress in this field is hindered partly by the current lack of direct measurements of the magnetic field in the solar corona and of other physical quantities such as plasma temperature and density that define the state of the coronal plasma, and partly by the very high complexity the solar corona exhibits as a dynamical system. Nevertheless, various methods have been developed during the past five decades for modelling the solar corona. The photospheric magnetic field measurements have been used as boundary conditions for such models. These models have different levels of sophistication, including different assumptions for the state of the coronal plasma and different requirements of computational resources. Deriving the coronal electric currents plays an important role in characterizing the different models. The simplest approach is to assume that no current exists within the corona, which leads to potential fields (Schatten, Wilcox, and Ness, 1969; Altschuler and Newkirk, 1969). Global potential fields require only line-of-sight (LOS) magnetic fields as the boundary. A popular approach for the outer boundary is the assumption of a source surface, where all field lines become parallel to the radial direction. This mimics the effect of stretching the field lines as a consequence of the solar wind flow. These are the so-called potential field source surface (PFSS) models. Schatten (1972) extended the PFSS model by introducing current sheets. Other global models take into account that the real coronal magnetic field has currents and is non-potential. Solving the full MHD equations for coronal modelling was done for axis-symmetric solutions in Mikić and Linker (1994) and in 3D in Mikić *et al.* (1999). MHD codes with an adaptive mesh refinement have been developed to study the solar corona including modelling the solar wind (Feng *et al.*, 2012b; Feng, 2020). Popular are also codes which solve subclasses of the full MHD equations, e.g., a special class of global magneto-hydro-static equilibria (see Bogdan and Low, 1986; Neukirch, 1995, for details) and stationary MHD including the solar wind flow (Wiegelmann *et al.*, 2020). For an overview on global coronal magnetic field models see the review articles by Mackay and Yeates (2012) and Wiegelmann, Petrie, and Riley (2017), and for force-free fields by Wiegelmann and Sakurai (2021).

Recent advances mainly within the last 15 years in both observational facilities like full-disk vector magnetograms from SOLIS (Synoptic Optical Long-term Investigations of the Sun) and the Helioseismic Magnetic Imager (HMI) on board the Solar Dynamics Observatory (SDO) and the increase of the available computational resources have contributed significantly to the improvement of the global corona models. Although there is still a lack of direct measurements of the coronal field, in contrast to the past, when only line-of-sight magnetograms were used, high-quality photospheric vector magnetograms can be employed now as more strict boundary conditions. Moreover, because of the recent advances in stereoscopy and the availability of high-resolution extreme-ultraviolet coronal images it is now possible to validate coronal magnetic field models, as was proposed by De Rosa *et al.* (2009) for Cartesian nonlinear force-free models. Observing coronal loops simultaneously from several vantage points allows us to reconstruct their 3D geometric structure by using stereoscopic techniques (see Aschwanden, 2011, for a review article on stereoscopy). Coronal observations can be used not only as a way to validate computational models, as done, e.g., in Yeates *et al.* (2018) but also as a tool to improve them, as demonstrated in Chifu, Wiegelmann, and Inhester (2017).

Currently, there are still limitations in deriving the full global structure of the coronal magnetic field. Two of the most significant challenges one has to face when constructing such global models are the quality of the vector magnetograms on the polar regions and the numerical inefficiencies associated with the convergence of the regular spherical grids towards the poles. The reliability of the vector magnetograms in these high latitude regions is questionable because of the large observation angle when the observations are performed from the ground (e.g. SOLIS) or spacecrafts orbiting within the ecliptic plane (e.g. SDO). As nonlinear force-free models require vector magnetograms as a boundary condition their applicability is not possible when the data

are not reliable. Furthermore, single finite-difference spherical grids suffer from numerical issues on the poles. More specifically, the convergence of the spherical grid towards the poles affects the convergence of the extrapolation algorithms. The successful launch of Solar Orbiter (SolO) in February of 2020 promises new measurements of the vector magnetic field on the solar polar regions. Recent overviews about the SoLo mission can be found in Zouganelis *et al.* (2020) and Rouillard *et al.* (2020). The Polarimetric and Helioseismic Imager (PHI) on board SolO will provide the magnetic field vector and the Extreme Ultraviolet Imager (EUI) EUV imaging observations of coronal loops. To be ready for the time when polar region vector magnetograms will become available, we developed a new code which can use these data as a boundary condition to compute the coronal global magnetic field. Our new code overcomes the problem of grid convergence in the polar regions because it is implemented on a Yin-Yang grid which is specifically developed for modeling spherical objects like planets, stars, etc. We structure the paper as follows. In Section 2 we give details of our new Yin-Yang code for computing nonlinear force-free fields (NLFFF), and in Section 3 we test our code with a semi-analytic reference solution while also examining its efficiency. Finally, we summarize our results and discuss our future research plans based on the newly developed code in Section 4.

2. Code description

2.1. Optimization code

Force-free magnetic fields are defined by both a vanishing Lorentz force and a vanishing magnetic field divergence. Therefore, they have to obey the following equations

$$(\nabla \times \mathbf{B}) \times \mathbf{B} = \mathbf{0}, \quad (1)$$

$$\nabla \cdot \mathbf{B} = 0. \quad (2)$$

One possibility to solve equations (1) and (2) was proposed by Wheatland, Sturrock, and Roumeliotis (2000) through the minimization of a functional L . For the study of global coronal magnetic fields, we use a functional expressed in spherical geometry as introduced in Wiegelmann (2007) and defined as

$$L = \int_V [B^{-2} |(\nabla \times \mathbf{B}) \times \mathbf{B}|^2 + |\nabla \cdot \mathbf{B}|^2] r^2 \sin \theta dr d\theta d\phi. \quad (3)$$

The definition of the functional (3) is such that $L = 0$ fulfils the requirement that the field is both force-free and divergence free, because the quadratic form in the functional ensures that equations (1) and (2) are satisfied for $L = 0$. The functional derivative of the functional leads to

$$\frac{\partial \mathbf{B}}{\partial t} = \mu \mathbf{F}, \quad (4)$$

where μ refers to a positive constant and the pseudo force \mathbf{F} is defined as

$$\begin{aligned} \mathbf{F} = & \nabla \times (\boldsymbol{\Omega}_a \times \mathbf{B}) - \boldsymbol{\Omega}_a \times (\nabla \times \mathbf{B}) \\ & + \nabla (\boldsymbol{\Omega}_b \cdot \mathbf{B}) - \boldsymbol{\Omega}_b (\nabla \cdot \mathbf{B}) + (\boldsymbol{\Omega}_a^2 + \boldsymbol{\Omega}_b^2) \mathbf{B} \end{aligned} \quad (5)$$

with

$$\boldsymbol{\Omega}_a = B^{-2} [(\nabla \times \mathbf{B}) \times \mathbf{B}] \quad (6)$$

$$\boldsymbol{\Omega}_b = B^{-2} [(\nabla \cdot \mathbf{B}) \mathbf{B}]. \quad (7)$$

A typical approach to solving nonlinear force-free equilibrium by minimizing equation (3) is to use a potential field as the initial state, which is a special class of a force-free equilibrium. Potential fields are usually not consistent with the horizontal magnetic field measurements, which are used as the bottom boundary for our model. Subsequently when calculating the functional (3) after having replaced the bottom layer of the potential field with the observed field, there is a (large) deviation of force- and divergence freeness. The functional L is then minimized numerically by applying the iterative equation (4). For the tests performed in this study, we use synthetic synoptic vector magnetograms and generalize the implementation of our spherical optimization code for synoptic magnetograms as described in Tadesse *et al.* (2014).

2.2. Yin-Yang grid

When the optimization algorithm is implemented on a regular finite difference spherical grid, there are some limitations when the computational domain extends towards the poles. Close to the polar regions, the spatial grid converges, which means that the minimum distance between the grid points decreases. The iteration step scales with the square of the spatial grid resolution and consequently the number of iteration steps until L reaches its minimum increases dramatically. The dynamic time step control in our previous spherical code (and also in the Cartesian code) decreases the time step automatically when L does not monotonously decrease. Consequently, the time step decreases by several orders of magnitude and the number of iterations steps until the convergence increases accordingly. Up to now, this limitation of the code was not significant for the application to currently available data, because the lack of reliable magnetic field measurements in solar polar regions did not allow accurate modelling of the coronal magnetic field above the poles anyway. Consequently, the computational domain was limited between 20 and 160 degrees in latitude to achieve a reasonable execution time. In the advent of polar magnetic field measurements from the Solar Orbiter mission, we implement the optimization code on a Yin-Yang grid to overcome the polar convergence issue. The Yin-Yang grid was introduced in Kageyama and Sato (2004) for geophysical applications. This overhead grid was to our knowledge first applied to solar applications by Jiang, Feng, and Xiang (2012) who implemented a Yin-Yang grid in their CESE-MHD code to compute nonlinear force-free fields equilibria by MHD relaxation. A Yin-Yang grid was also implemented in the AMR-CESE-MHD code to study the global coronal evolution in a data-driven model by Feng *et al.* (2012a). The Yin-Yang grid consists of two identical spherical grids. The first component of the grid is a regular spherical grid with some cutout regions. More specifically, $\frac{\pi}{4} < \theta < \frac{3\pi}{4}$ and $\frac{\pi}{4} < \phi < \frac{7\pi}{4}$, which corresponds to $45^\circ < \theta < 135^\circ$ and $45^\circ < \phi < 315^\circ$ (θ refers to the longitude and ϕ to the latitude). The other component of the grid is the Yang grid, which is identical to the complementary Yin grid and perpendicular to it. While both grids do not have polar regions, the two combined grids cover the entire sphere. The spherical grids are defined close enough to the equatorial regions so that the finite difference grid is almost equidistant. This allows the use of a larger iteration step. The prize one has to pay is that the boundaries of each grid should be updated to capture the evolution of the field that happens within the other grid. This should be done while the optimization algorithm is running thus increasing the algorithm complexity. The corresponding coordinate transformation equations between the two grids are given by

$$r^e = r^n, \tag{8}$$

$$\sin \theta^e \cos \phi^e = -\sin \theta^n \cos \phi^n, \tag{9}$$

$$\sin \theta^e \sin \phi^e = \cos \theta^n, \tag{10}$$

$$\cos \theta^e = \sin \theta^n \sin \phi^n, \tag{11}$$

where the index e is used to refer to the Yin grid and the index n to the Yang grid. As the two-component grids are completely symmetrical to each other, the same expression is used to transform coordinates from the Yang to the Yin grid. The symmetry of the two grids is very convenient for the implementation of the code, because all mathematical and algorithmic procedures can operate on both grids.

2.3. Yin-Yang implementation

There are two basic differences between the previous version of the optimization code and the newly developed one. All numerical operations called to operate on one grid are also called to operate on the other. The lateral boundaries of each grid (which have been fixed to a potential field in previous code versions) are now updated with values taken from the complementary grid. In this way, the new method overcomes the problem of earlier codes where the lateral boundaries were required to be specified. The Yin-Yang implementation requires only boundary conditions at the photosphere and on the outer boundary. In order to update the boundaries of one grid using the values from the other, we apply the following procedure:

1. For an arbitrary grid point, we perform a coordinate transformation to find its coordinates with respect to the other grid.
2. Compute the magnetic field vector at this point, by applying an interpolation method. It is important to note here that the new coordinates of our arbitrary point do not have to match with the coordinates of a grid point of the other grid and this is why we have to interpolate to estimate the components of the magnetic field vector.
3. Transform the magnetic vector back to the initial grid.

Because of the symmetry of the grids, this process is identical regardless of which is the first and second grid. We describe below all the steps needed for the new Yin-Yang optimization code.

1. Initialize the Yin grid by performing a potential extrapolation using the line of sight magnetogram as a boundary condition.
2. Replace the bottom boundary of the Yin grid with a vector magnetogram. Here, a synthetic one deduced from the Low and Lou solution is used.
3. Initialize the Yang grid by coordinate transformation, interpolation and vector transformation.
4. Calculate L with equation (3) separately on both grids.
5. Add $L = L_{\text{Yin}} + L_{\text{Yang}}$.
6. The iterative equation (4) is used to iterate the field towards minimizing L separately on both grids.
7. The boundaries of each grid are updated using the values of the field on the other grid (by coordinate transformation, interpolation, and vector transformation).
8. The code is terminated when L becomes stationary.
9. The final solution can be transformed to both grids.

3. Validation of the code

3.1. Method

In this section, we want to evaluate the performance of our newly developed code. The aim is to find out whether our code is able to minimize the functional L down to numerical precision and to compare the output of our code with a known nonlinear force-free field reference equilibrium. Checking the force-freeness and comparing with a reference solution are standard procedures to

validate NLFFF codes implemented on Cartesian and spherical grids. A frequently used reference solution for this aim is a semi-analytical nonlinear force-free equilibrium solution found by Low and Lou (1990). This method solves a Grad-Shafranov equation in spherical coordinates, which is invariant in the ϕ -direction, but displacements of the origin and rotation allows to compute equilibria which change in all three spatial coordinates. It can be used to evaluate nonlinear force-free codes in 3D (as done for Cartesian geometry in, e.g., Wiegelmann, 2004; Amari, Boulmezaoud, and Aly, 2006; Schrijver *et al.*, 2006; Inhester and Wiegelmann, 2006; Valori, Kliem, and Fuhrmann, 2007) and to evaluate spherical NLFFF codes (Wiegelmann, 2007; Song *et al.*, 2007; Tadesse, Wiegelmann, and Inhester, 2009; Jiang, Feng, and Xiang, 2012; Guo *et al.*, 2012; Contopoulos, 2013; Amari *et al.*, 2013). Following these works, we use a spherical Low and Lou solution as reference to evaluate our code, which we do as described below.

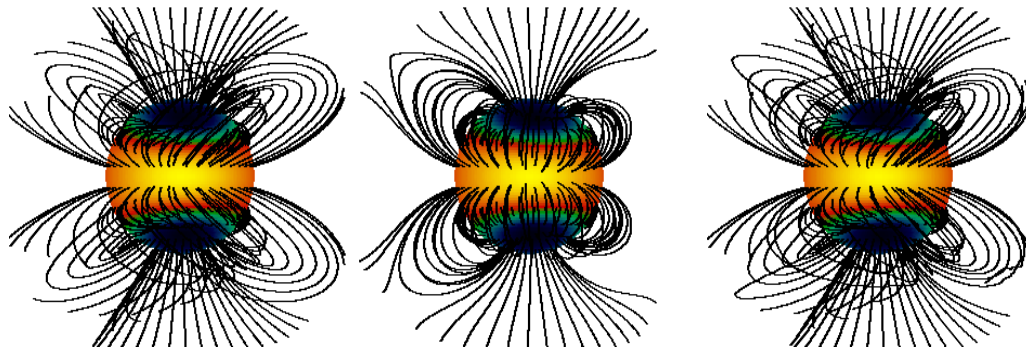


Figure 1. A comparison of some magnetic field lines. The left panel shows the Low and Lou reference solution, the center panel the initial PFSS field and the right panel the output from our code.

1. Calculate the spherical Low and Lou solution in 3D which from now on we will call the reference solution. A field line plot for this reference solution is shown in Figure 1, left panel. The reference solution was computed on a spherical grid with $n_r = 45$, $n_\theta = 90$, and $n_\phi = 180$ where n_r is the number of points in the radial direction, n_θ is the number of points in latitude, and n_ϕ is the number of points in longitude.
2. By using the radial component of the Low and Lou solution as a synthetic magnetogram, we performed a potential field extrapolation on the same spherical grid, which is shown in Figure 1, middle panel.
3. We use the potential field as computed in the last step as initial equilibrium and the bottom boundary from the reference solution is taken as a synthetic vector map used as a boundary condition for our new code. The top boundary was selected to be either the top boundary of the potential field or the top boundary from the reference field. The effect of using these different top boundary conditions will be examined in section 3.2.
4. We run the optimization code and compare the results with the reference Low and Lou solution and evaluate the influence of several effects as stated below. A visual representation of one of our outputs (duplicated case 3, see also Table 1) is shown in Figure 1, right panel.

3.2. Code specifications and free parameters

A number of different parameters are used in order to control the flow of the code and to specify different conditions, as explained below. How these specifications influence the quality and computing time of our code are presented in Table 1.

1. Interpolation method: Specifies the order of the interpolation method used during the vector transformation process. As a first test, we use a bi-linear interpolation. Please note that the r is always identical on both grids and interpolation is needed only for the lateral directions. In principle, higher-order interpolation methods could be used.
2. Non-interpolation steps (NIS): Defines the number of optimization steps between updating the boundaries of the one grid with vectors interpolated and transformed from the other grid.
3. The initial iteration step is $\mu = 10^{-4}$, which is sufficiently small to ensure a strictly decreasing functional L if μ is kept constant.
4. Iteration step reducer: This parameter divides μ if the functional L does not decrease after one iteration step. This is considered as a non-successful iteration step, which is refused and repeated with the reduced iteration step when running the code with a dynamically controlled time step.
5. Iteration step increaser: This parameter multiplies μ with 1.01 after every successful iteration step. This doubles the iteration step after 70 successful iterations. The optimization ensures a continuous decrease of L (see Wheatland, Sturrock, and Roumeliotis, 2000). In a numerical implementation L can increase if the iteration time step is too large. The time-step increaser and reducer help to search for the optimum time-step, as high as possible (for a short computing time) and as low as necessary (to ensure a strictly monotonously decreasing L). The code is terminated either when the maximum number of iterations is reached or when μ becomes smaller than a threshold number 10^{-9} .
6. The original Yin & Yang grid spans in the range $45 \leq \theta \leq 135$ and $45 \leq \phi \leq 315$. In most cases we use this standard grid, but we investigate also the effect of different (non-standard) grids.

3.3. First qualitative evaluation

Our first tool to validate our new code is the comparison between the field lines of the solution resulting from our code with the field lines of the reference solution and the potential solution as shown in Figure 1. It is evident from the reference solution in the left panel that the output of our code depicts a very good qualitative agreement of the corresponding magnetic field lines. The potential field model, which was used as the initial equilibrium for our code shows large deviations in the field line plots.

3.4. Quantitative evaluation

Visualizing our solution and comparing the corresponding magnetic field line plots with the reference solution as done in Figure 1 is a fast way to qualitatively evaluate our results. Here we use a number of quantitative criteria. The value of the functional L (equation 3) after the optimization evaluates how close is the resulting field to a force free and divergence free state. We compute this also separately for the Lorentz-force part, defined as

$$L_1 = \int_V [B^{-2} |(\nabla \times \mathbf{B}) \times \mathbf{B}|^2] r^2 \sin \theta dr d\theta d\phi, \quad (12)$$

and the divergence integral defined as

$$L_2 = \int_V |\nabla \cdot \mathbf{B}|^2 r^2 \sin \theta dr d\theta d\phi. \quad (13)$$

Additionally, we compare our results quantitatively with the reference resolution by a number of quantitative measures, (as introduced in Schrijver *et al.*, 2006).

Namely we use the Vector Correlation which is defined as

$$VC = \sum_i \mathbf{B}_i \cdot \mathbf{b}_i / \left(\sum_i |\mathbf{B}_i|^2 \sum_i |\mathbf{b}_i|^2 \right)^{1/2}, \quad (14)$$

and the Energy Percentage defined as

$$EP = \frac{\sum_i |\mathbf{b}_i|^2}{\sum_i |\mathbf{B}_i|^2} \quad (15)$$

The magnetic field output from our code \mathbf{b}_i is compared to a reference solution \mathbf{B}_i (here the Low and Lou solution). For a perfect agreement of our solutions with the reference, both quantities should be unity. In order to compute these numerical quantities, the sums are taken over all N data points of the computational grid. More specifically, for the computation of each quantity, we calculate the Yin and the Yang part separately and then average them weighted with the number of points used for the computation in the respective grid. In order to not include the overlapping regions, twice in the computations for these regions we use the points of the Yin grid and this is why there is the need for these weighted averaging. The vector correlation VC is an important indicator, of how well the two vector fields agree because it involves the dot products between the vectors as well as their magnitudes. The percentage of the magnetic energy EP not only helps us to compare the two vector fields but also has a physical meaning. If the energy in our solution is not close to the energy of the reference solution our model is not that useful because being able to calculate the free magnetic energy stored in the corona is one of the reasons why nonlinear force-free extrapolations are useful. Having the energy percentage close to unity tells us that overall the vectors of our vector field have the correct magnitude.

3.5. Comparison of different test cases

- Case 0: In this case the initial potential field and the discretization error (L, L1, and L2) are computed. This does not require optimisation, but only one iteration to compute the functional L . A comparison with the reference solution is done as well. All comparison criteria should be close to their ideal values so that the potential-field solution is meaningful.
- Case 1: This case estimates the discretization error of the reference solution computed on the numerical grids. Again, no iteration was done, just one evaluation of L was computed.
- Cases 2–4: These are the first real tests which use an initial potential field and both the bottom and top boundaries are prescribed from the reference solution. This ensures fully consistent boundary conditions. This set-up of boundary conditions for the Yin-Yang code is equivalent as prescribing all six boundaries of the computational box of a Cartesian NLFFF code. All quantities show an almost perfect agreement with the reference solution (Case 1). The values of L, L1, and L2 are even a bit smaller than the discretization error of the semi-analytical reference field. The reason for this is that the code optimizes these quantities on the numerical grids. The results are not affected if the update of the boundaries between the Yin and Yang grid is done after every iteration step (Case 2) or only after every 10 or 100 iteration steps as in Cases 3 and 4, respectively. When examining the convergence of the code, it seems that in Case 2 it converges faster than in Case 3 and in Case 3 it converges faster than in Case 4. This can be understood as more frequent update of the boundaries that insures faster flow of information between the grids. When we talk about convergence speed we refer to the number of iterations needed to reduce L . The difference in convergence speed is so small that it is not visible in Figure 3. A significant difference

Table 1. The table summarizes the specifications of our test cases (columns 1 – 4) and a quantitative evaluation of the results (columns 5 – 11). The first column ‘Case’ names the test cases. The second column ‘NIS’ the Non-Interpolation-Steps. This means the number of iterations are done on the Yin and Yang separately without communication between the two grids. Column three ‘Bound’ specifies the used boundary condition. Here ‘l’ means that the Low & Lou reference field was specified in the photosphere and on the outer boundary and ‘p’ means that a potential field was specified on the outer boundary. Column four ‘ μ control’ specifies whether a constant iteration time step was used (value 1) or if and how the time-step was controlled dynamically (see the text for details). Column five ‘Iterations’ shows the number of iteration steps until convergence and column six ‘Time’, the computational time in minutes on Mac book pro with M1 processor. Columns seven to nine ‘L’, ‘L1’, ‘L2’ show the final value of the minimized functional L (see equation (3)) and its two parts which are the residual Lorentz force (see equation(12)) and the residual magnetic field divergence (see equation (13)). Finally, we compare the output of our code with the reference solution by the vector correlation (see equation (14)) in column ten ‘VC’ and the energy percentage (see equation(15)) in column eleven named ‘EP’.

Case	NIS	Bound	μ control	Iterations	Time	L	L1	L2	VC	EP
Cases 1 – 7 with constant iteration time step μ										
Yin & Yang grid with $45 \leq \theta \leq 135$ and $45 \leq \phi \leq 315$										
0	1	p	-	1	< 1	0.001	0.001	0.000	0.876	0.783
1	1	l	-	1	< 1	0.025	0.012	0.012	1.000	1.000
2	1	l	-	40000	248	0.013	0.010	0.004	1.000	0.998
3	10	l	-	40000	190	0.013	0.010	0.004	1.000	0.998
4	100	l	-	40000	186	0.014	0.011	0.004	1.000	0.998
5	1	p	-	31340	166	0.070	0.048	0.022	0.996	0.957
6	10	p	-	31960	149	0.070	0.048	0.023	0.996	0.957
7	100	p	-	35100	163	0.070	0.048	0.023	0.996	0.958
Cases 8 – 13 with dynamical controlled iteration time step μ										
Yin & Yang grid with $45 \leq \theta \leq 135$ and $45 \leq \phi \leq 315$										
8	1	l	2.0	5763	30	0.047	0.032	0.015	0.998	0.972
9	1	l	1.5	5695	31	0.038	0.026	0.012	0.998	0.977
10	1	l	1.25	4319	23	0.061	0.041	0.019	0.997	0.965
11	1	p	2.0	7221	37	0.084	0.061	0.023	0.994	0.942
12	1	p	1.5	7213	39	0.084	0.061	0.023	0.994	0.942
13	1	p	1.25	6956	37	0.084	0.061	0.023	0.994	0.942
Case 14 with Yin & Yang grid with $50 \leq \theta \leq 130$ and $35 \leq \phi \leq 325$										
14	1	l	2	4756	25	0.246	0.190	0.057	0.996	0.961
Case 15 with Yin & Yang grid with $35 \leq \theta \leq 145$ and $55 \leq \phi \leq 305$										
15	1	l	2	27618	134	0.221	0.173	0.049	0.997	0.974

is observed in the computational time which is reduced by about 25% as the updating of the boundaries is a lot less frequent in these cases. The reduction of the execution time is not that significant when going from 10 to 100 non-interpolation steps as the percentage of the execution time that the code spends on doing the updates is a lot smaller in Case 3 than in Case 2. In all cases, a fixed (small) iteration time-step was used and the code was running until the maximum number of allowed steps (40 000) was reached. The evolution of L (a decrease of almost four orders of magnitude) during the iterations is shown in Figure 2 and the development of the vector correlation and energy percentage in Figure 3. These two quantities naturally start with the potential field values and reach almost one at the end of the iteration.

-
- Cases 5–7: They are similar to Cases 2–4 with the only difference that the bottom boundary of our computational domain was prescribed by the reference solution. The outer boundary was taken from the initial potential-field solution. These two boundaries are not necessarily consistent with each other. However, these test cases are closer to the code application real observational data. When a full-Sun extrapolation is attempted, only photospheric magnetic field measurements are available at present and the outer boundary is a priori unknown. This set-up of boundary conditions is comparable to specifying only the bottom boundary of a Cartesian code. The inconsistent top and bottom boundary result in slightly increased residual L , $L1$, and $L2$, a still almost perfect vector correlation, and an error of about 4% in the magnetic energy. Again the number of non-interpolation steps hardly influenced the result. updating the interpolation only every 10 steps resulted in the lowest computing time, but not by a large margin. In order to understand this difference is important to mention here that in Case 6 fewer iterations were needed to reach the state with a minimum L compared to Case 7. This is expected as the more frequent update of the boundaries ensures faster communication between the grids, thus accelerating the convergence. On the other hand, the code runs faster when the updates are not that frequent. Therefore, the combination of these two competing procedures gives us this complex dynamics.
 - Cases 8–10: Here, instead of using a fixed small iteration step, we controlled the iteration step dynamically. If both bottom and top boundaries are prescribed, we get a slight increase in the residual errors L , $L1$, and $L2$ compared with a fixed time step and an error in the energy percentage of 3 – 4%. The vector correlation is almost one. Compared with a fixed time step, we obtain a drastically reduced computational time by a factor of about ten.
 - Cases 11–13: Here, we explore the dynamic time step control for the realistic case in which only the photospheric magnetic field is provided. The effects of potential inconsistent bottom and outer boundaries and the effects of the dynamic control of time step cumulate in a slightly higher residual error in $L1$, but not in $L2$. Compared with the fixed time-step computation, the error in the energy percentage increases by another 1.5% and the magnetic energy is underestimated by almost 6% compared with the reference solution. The computing time decreases by a factor of about four compared to the cases with a fixed time step.
 - Cases 14 and 15: Here, we investigate the effect of a non-standard Yin-Yang grid and changed the areas where both grids overlap. This was done for a case with a dynamically controlled time step and the top boundary taken from the reference solution. All quantities (residual L , $L1$, and $L2$ and comparison matrices VC and EP) compare worse with the standard Yin-Yang grid, and consequently, we do not investigate further non-standard grids.

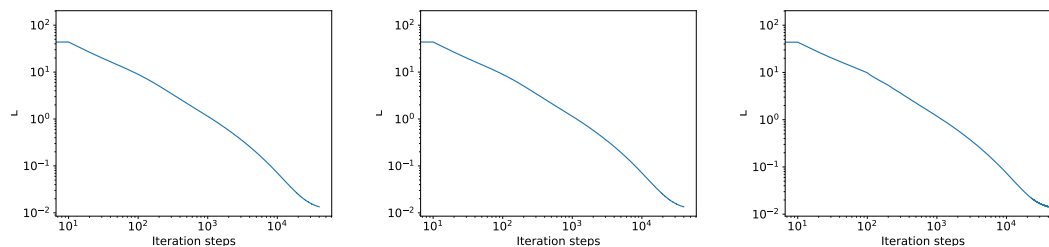


Figure 2. Visualizing minimization of functional L from left to right cases 2, 3, and 4.

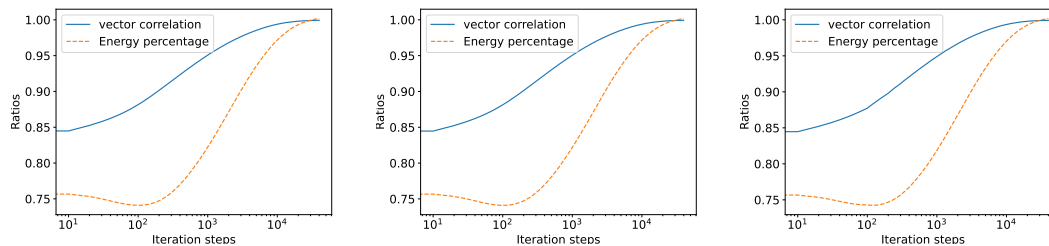


Figure 3. Evolution of the vector correlation and normalized magnetic energy from left to right cases 2, 3, and 4.

4. Conclusion and future plans

We developed a new nonlinear force-free optimization code implemented on a Yin-Yang grid. The quality of the solutions is comparable to the ones produced by a previous version of the spherical NLFFF code as described in Wiegelmann (2007). Please note that the previous code version did not include proper treatment of the polar regions and the tests have been done on a lower resolution grid. Within this work, we investigated the influence of several code specifications. The first more technical test was to investigate the new code under the condition of complete and consistent boundary conditions, where the reference solution was specified on all boundaries, which showed an almost perfect agreement of the computed equilibria with the reference solution. Please note that the Yin & Yang grids have no lateral boundaries and only bottom and top boundaries needed to be prescribed. On the Sun, we have, however, only magnetic field measurements in the photosphere and other boundaries are unknown. A natural guess is using a potential field source surface model to prescribe the boundary conditions on the source surface. Our code does still provide a good agreement with the reference solution. The vector correlation with the reference solution has an error of about 0.5% and the error in the magnetic energy is in the range of 4% (for a fixed small time step) and 6% (for a dynamically controlled time step). A dynamic time step does, however, reduce the computing time by about a factor of 4.5. We also investigated to which extent the final result is influenced by how often the Yin grid and Yang grid communicate which each other (after every iteration step, after 10 and after 100 steps) and it was found that these hardly influence the solution. The lowest computing time was reached if the interpolation between the two grids was done every tenth iteration step. From this, we conclude that using a dynamically controlled time step and grid communication at every tenth step should be the standard for future application to data. If computing time does not matter a small fixed time step gives somewhat more accurate results. Our next plans are to apply our new code to the forthcoming synoptic vector magnetograms created by observations from SoLo/PHI and SDO/HMI data. The high orbit from SoLo allows a view of the poles and combining data from both spacecrafts will allow to remove the 180-degree ambiguity by stereoscopy (as investigated in Valori *et al.*, 2022). Our newly developed Yin-Yang implementation is timely for an application to these new vector maps, which are expected to be more accurate than the current data (due to the stereoscopic ambiguity removal approach) and because polar fields will be measured. We would like to point out that the resulting full sphere global coronal magnetic field model is not only important as a stand-alone result, but knowing the global magnetic topology and connectivity helps also to prescribe (lateral and top) boundary conditions for local computations, e.g. in active regions and at the poles.

Acknowledgments AK acknowledges IMPRS as this work was supported by the International Max-Planck Research School (IMPRS) for Solar System Science at the University of Göttingen. TW acknowledges financial

support by DLR-grant 50 OC 2101. The authors thank Maria S. Madjarska and Bernd Inhester for the discussions and useful comments to the manuscript.

Disclosure of potential conflict of interest: The authors declare that they have no conflicts of interest.

References

- Altschuler, M.D., Newkirk, G.: 1969, Magnetic Fields and the Structure of the Solar Corona. I: Methods of Calculating Coronal Fields. *Solar Phys.* **9**(1), 131. DOI. ADS.
- Amari, T., Boulmezaoud, T.Z., Aly, J.J.: 2006, Well posed reconstruction of the solar coronal magnetic field. *Astron. Astrophys.* **446**(2), 691. DOI. ADS.
- Amari, T., Aly, J.-J., Canou, A., Mikic, Z.: 2013, Reconstruction of the solar coronal magnetic field in spherical geometry. *Astron. Astrophys.* **553**, A43. DOI. ADS.
- Aschwanden, M.J.: 2011, Solar Stereoscopy and Tomography. *Living Reviews in Solar Physics* **8**(1), 5. DOI. ADS.
- Bogdan, T.J., Low, B.C.: 1986, The three-dimensional structure of magnetostatic atmospheres. II - Modeling the large-scale corona. *Astrophys. J.* **306**, 271. DOI. ADS.
- Chifu, I., Wiegmann, T., Inhester, B.: 2017, Nonlinear Force-free Coronal Magnetic Stereoscopy. *Astrophys. J.* **837**, 10. DOI. ADS.
- Contopoulos, I.: 2013, The Force-Free Electrodynamics Method for the Extrapolation of Coronal Magnetic Fields from Vector Magnetograms. *Solar Phys.* **282**(2), 419. DOI. ADS.
- De Rosa, M.L., Schrijver, C.J., Barnes, G., Leka, K.D., Lites, B.W., Aschwanden, M.J., Amari, T., Canou, A., McTiernan, J.M., Régnier, S., Thalmann, J.K., Valori, G., Wheatland, M.S., Wiegmann, T., Cheung, M.C.M., Conlon, P.A., Fuhrmann, M., Inhester, B., Tadesse, T.: 2009, A Critical Assessment of Nonlinear Force-Free Field Modeling of the Solar Corona for Active Region 10953. *Astrophys. J.* **696**(2), 1780. DOI. ADS.
- Feng, X.: 2020, *Magnetohydrodynamic Modeling of the Solar Corona and Heliosphere*. DOI.
- Feng, X., Jiang, C., Xiang, C., Zhao, X., Wu, S.T.: 2012a, A Data-driven Model for the Global Coronal Evolution. *Astrophys. J.* **758**(1), 62. DOI. ADS.
- Feng, X., Yang, L., Xiang, C., Jiang, C., Ma, X., Wu, S.T., Zhong, D., Zhou, Y.: 2012b, Validation of the 3D AMR SIP-CESE Solar Wind Model for Four Carrington Rotations. *Solar Phys.* **279**(1), 207. DOI. ADS.
- Guo, Y., Ding, M.D., Liu, Y., Sun, X.D., DeRosa, M.L., Wiegmann, T.: 2012, Modeling Magnetic Field Structure of a Solar Active Region Corona Using Nonlinear Force-free Fields in Spherical Geometry. *Astrophys. J.* **760**(1), 47. DOI. ADS.
- Inhester, B., Wiegmann, T.: 2006, Nonlinear Force-Free Magnetic Field Extrapolations: Comparison of the Grad Rubin and Wheatland Sturrock Roumeliotis Algorithm. *Solar Phys.* **235**(1-2), 201. DOI. ADS.
- Jiang, C., Feng, X., Xiang, C.: 2012, A New Code for Nonlinear Force-free Field Extrapolation of the Global Corona. *Astrophys. J.* **755**(1), 62. DOI. ADS.
- Kageyama, A., Sato, T.: 2004, “Yin-Yang grid”: An overset grid in spherical geometry. *Geochemistry, Geophysics, Geosystems* **5**(9), Q09005. DOI. ADS.
- Low, B.C., Lou, Y.Q.: 1990, Modeling Solar Force-free Magnetic Fields. *Astrophys. J.* **352**, 343. DOI. ADS.
- Mackay, D.H., Yeates, A.R.: 2012, The Sun’s Global Photospheric and Coronal Magnetic Fields: Observations and Models. *Living Reviews in Solar Physics* **9**, 6. DOI. ADS.
- Mikic, Z., Linker, J.A.: 1994, Disruption of Coronal Magnetic Field Arcades. *Astrophys. J.* **430**, 898. DOI. ADS.
- Mikić, Z., Linker, J.A., Schnack, D.D., Lionello, R., Tarditi, A.: 1999, Magnetohydrodynamic modeling of the global solar corona. *Physics of Plasmas* **6**(5), 2217. DOI. ADS.
- Neukirch, T.: 1995, On self-consistent three-dimensional analytic solutions of the magnetohydrostatic equations. *Astron. Astrophys.* **301**, 628. ADS.
- Rouillard, A.P., Pinto, R.F., Vourlidas, A., De Groof, A., Thompson, W.T., Bemporad, A., Dolei, S., Indurain, M., Buchlin, E., Sasso, C., Spadaro, D., Dalmasse, K., Hirzberger, J., Zouganelis, I., Strugarek, A., Brun, A.S., Alexandre, M., Berghmans, D., Raouafi, N.E., Wiegmann, T., Pagano, P., Arge, C.N., Nieves-Chinchilla, T., Lavarra, M., Poirier, N., Amari, T., Aran, A., Andretta, V., Antonucci, E., Anastasiadis, A., Auchère, F., Bellot Rubio, L., Nicula, B., Bonnin, X., Bouchemit, M., Budnik, E., Caminade, S., Cecconi, B., Carlyle, J., Cernuda, I., Davila, J.M., Etesi, L., Espinosa Lara, F., Fedorov, A., Fineschi, S., Fludra, A., Génot, V., Georgoulis, M.K., Gilbert, H.R., Giunta, A., Gomez-Herrero, R., Guest, S., Haberleiter, M., Hassler, D., Henney, C.J., Howard, R.A., Horbury, T.S., Janvier, M., Jones, S.I., Kozarev, K., Kraaikamp, E., Kouloumvakos, A., Krucker, S., Lagg, A., Linker, J., Lavraud, B., Louarn, P., Maksimovic, M., Maloney, S., Mann, G., Masson, A., Müller, D., Önel, H., Osuna, P., Orozco Suarez, D., Owen, C.J., Papaioannou, A., Pérez-Suárez, D., Rodríguez-Pacheco, J., Parenti, S., Pariat, E., Peter, H., Plunkett, S., Pomoell, J., Raines, J.M., Riethmüller, T.L., Rich, N., Rodríguez, L., Romoli, M., Sanchez, L., Solanki, S.K., St Cyr, O.C., Straus, T., Susino, R., Teriaca, L., del Toro Iniesta, J.C., Ventura, R., Verbeeck, C., Vilmer, N., Warmuth, A., Walsh, A.P., Watson, C., Williams, D., Wu, Y., Zhukov, A.N.: 2020, Models and data analysis tools for the Solar Orbiter mission. *Astron. Astrophys.* **642**, A2. DOI. ADS.

- Schatten, K.H.: 1972, Current Sheet Magnetic Model for the Solar Corona. In: Sonett, C.P., Coleman, P.J., Wilcox, J.M. (eds.) *NASA Special Publication* **308**, 44. ADS.
- Schatten, K.H., Wilcox, J.M., Ness, N.F.: 1969, A model of interplanetary and coronal magnetic fields. *Solar Phys.* **6**(3), 442. DOI. ADS.
- Schrijver, C.J., De Rosa, M.L., Metcalf, T.R., Liu, Y., McTiernan, J., Régnier, S., Valori, G., Wheatland, M.S., Wiegmann, T.: 2006, Nonlinear Force-Free Modeling of Coronal Magnetic Fields Part I: A Quantitative Comparison of Methods. *Solar Phys.* **235**(1-2), 161. DOI. ADS.
- Song, M.T., Fang, C., Zhang, H.Q., Tang, Y.H., Wu, S.T., Zhang, Y.A.: 2007, Reconstructing Spherical Nonlinear Force-free Field in the Solar Corona. *Astrophys. J.* **666**(1), 491. DOI. ADS.
- Tadesse, T., Wiegmann, T., Inhester, B.: 2009, Nonlinear force-free coronal magnetic field modelling and preprocessing of vector magnetograms in spherical geometry. *Astron. Astrophys.* **508**(1), 421. DOI. ADS.
- Tadesse, T., Wiegmann, T., Gosain, S., MacNeice, P., Pevtsov, A.A.: 2014, First use of synoptic vector magnetograms for global nonlinear, force-free coronal magnetic field models. *Astron. Astrophys.* **562**, A105. DOI. ADS.
- Valori, G., Kliem, B., Fuhrmann, M.: 2007, Magnetofrictional Extrapolations of Low and Lou's Force-Free Equilibria. *Solar Phys.* **245**(2), 263. DOI. ADS.
- Valori, G., Löschl, P., Stansby, D., Pariat, E., Hirzberger, J., Chen, F.: 2022, Disambiguation of Vector Magnetograms by Stereoscopic Observations from the Solar Orbiter (SO)/Polarimetric and Helioseismic Imager (PHI) and the Solar Dynamic Observatory (SDO)/Helioseismic and Magnetic Imager (HMI). *Solar Phys.* **297**(1), 12. DOI. ADS.
- Wheatland, M.S., Sturrock, P.A., Roumeliotis, G.: 2000, An Optimization Approach to Reconstructing Force-free Fields. *Astrophys. J.* **540**(2), 1150. DOI. ADS.
- Wiegmann, T.: 2004, Optimization code with weighting function for the reconstruction of coronal magnetic fields. *Solar Phys.* **219**(1), 87. DOI. ADS.
- Wiegmann, T.: 2007, Computing Nonlinear Force-Free Coronal Magnetic Fields in Spherical Geometry. *Solar Phys.* **240**(2), 227. DOI. ADS.
- Wiegmann, T., Sakurai, T.: 2021, Solar force-free magnetic fields. *Living Reviews in Solar Physics* **18**(1), 1. DOI. ADS.
- Wiegmann, T., Petrie, G.J.D., Riley, P.: 2017, Coronal Magnetic Field Models. *Space Sci. Rev.* **210**, 249. DOI. ADS.
- Wiegmann, T., Neukirch, T., Nickeler, D.H., Chifu, I.: 2020, An Optimization Principle for Computing Stationary MHD Equilibria with Solar Wind Flow. *Solar Phys.* **295**(10), 145. DOI. ADS.
- Yeates, A.R., Amari, T., Contopoulos, I., Feng, X., Mackay, D.H., Mikić, Z., Wiegmann, T., Hutton, J., Lowder, C.A., Morgan, H., Petrie, G., Rachmeler, L.A., Upton, L.A., Canou, A., Chopin, P., Downs, C., Druckmüller, M., Linker, J.A., Seaton, D.B., Török, T.: 2018, Global Non-Potential Magnetic Models of the Solar Corona During the March 2015 Eclipse. *Space Sci. Rev.* **214**, 99. DOI. ADS.
- Zouganelis, I., De Groof, A., Walsh, A.P., Williams, D.R., Müller, D., St Cyr, O.C., Auchère, F., Berghmans, D., Fludra, A., Horbury, T.S., Howard, R.A., Krucker, S., Maksimovic, M., Owen, C.J., Rodríguez-Pacheco, J., Romoli, M., Solanki, S.K., Watson, C., Sanchez, L., Lefort, J., Osuna, P., Gilbert, H.R., Nieves-Chinchilla, T., Abbo, L., Alexandrova, O., Anastasiadis, A., Andretta, V., Antonucci, E., Appourchaux, T., Aran, A., Arge, C.N., Aulanier, G., Baker, D., Bale, S.D., Battaglia, M., Bellot Rubio, L., Bemporad, A., Berthomier, M., Bocchialini, K., Bonnin, X., Brun, A.S., Bruno, R., Buchlin, E., Büchner, J., Bucik, R., Carcaboso, F., Carr, R., Carrasco-Blázquez, I., Cecconi, B., Cernuda Cangas, I., Chen, C.H.K., Chitta, L.P., Chust, T., Dalmasse, K., D'Amicis, R., Da Deppo, V., De Marco, R., Dolei, S., Dolla, L., Dudok de Wit, T., van Driel-Gesztelyi, L., Eastwood, J.P., Espinosa Lara, F., Etesi, L., Fedorov, A., Félix-Redondo, F., Fineschi, S., Fleck, B., Fontaine, D., Fox, N.J., Gandorfer, A., Génot, V., Georgoulis, M.K., Gissot, S., Giunta, A., Gizon, L., Gómez-Herrero, R., Gontikakis, C., Graham, G., Green, L., Grundy, T., Haberberger, M., Harra, L.K., Hassler, D.M., Hirzberger, J., Ho, G.C., Hurford, G., Innes, D., Issautier, K., James, A.W., Janitzek, N., Janvier, M., Jeffrey, N., Jenkins, J., Khotyaintsev, Y., Klein, K.-L., Kontar, E.P., Kontogiannis, I., Krafft, C., Krasnoselskikh, V., Kretzschmar, M., Labrosse, N., Lagg, A., Landini, F., Lavraud, B., Leon, I., Lepri, S.T., Lewis, G.R., Liewer, P., Linker, J., Livi, S., Long, D.M., Louarn, P., Malandraki, O., Maloney, S., Martinez-Pillet, V., Martinovic, M., Masson, A., Matthews, S., Matteini, L., Meyer-Vernet, N., Moraitis, K., Morton, R.J., Musset, S., Nicolaou, G., Nindos, A., O'Brien, H., Orozco Suarez, D., Owens, M., Pancrazzi, M., Papaioannou, A., Parenti, S., Pariat, E., Patsourakos, S., Perrone, D., Peter, H., Pinto, R.F., Plainaki, C., Plettmeier, D., Plunkett, S.P., Raines, J.M., Raouafi, N., Reid, H., Retino, A., Rezeau, L., Rochus, P., Rodriguez, L., Rodriguez-Garcia, L., Roth, M., Rouillard, A.P., Sahrquai, F., Sasso, C., Schou, J., Schühle, U., Sorriso-Valvo, L., Soucek, J., Spadaro, D., Stangalini, M., Stansby, D., Steller, M., Strugarek, A., Štverák, Š., Susino, R., Telloni, D., Terasa, C., Teriaca, L., Toledo-Redondo, S., del Toro Iniesta, J.C., Tsiropoula, G., Tsounis, A., Tziotziou, K., Valentini, F., Vaivads, A., Vecchio, A., Velli, M., Verbeek, C., Verdini, A., Verscharen, D., Vilmer, N., Vourlidas, A., Wicks, R., Wimmer-Schweingruber, R.F., Wiegmann, T., Young, P.R., Zhukov, A.N.: 2020, The Solar Orbiter Science Activity Plan. Translating solar and heliospheric physics questions into action. *Astron. Astrophys.* **642**, A3. DOI. ADS.